JOURNAL OF THERMOPHYSICS AND HEAT TRANSFER
Vol. 16, No. 1, January–March 2002

Ground Testing Facility for Modeling Real Projectile Flight Heating in Earth Atmosphere

Friedrich Seiler,* Udo Werner,† and Gunther Patz‡
French–German Research Institute of Saint-Louis, F-68301 Saint-Louis, France

An analytical method for obtaining the heating of a hypersonic projectile with a conical forebody and data obtained from a special ballistic range to validate the method are presented. The method is a classical boundary-layer technique for turbulent flow. It involves a coordinate transformation that enables flat plate solutions to be adapted to the conical coordinates. The heating to the projectile nose cone was then obtained analytically with a semi-infinite slab, according to the given boundary conditions for flow velocity and gas temperature. The laminar–turbulent transition in the cone boundary layer takes place some millimeters downstream of the tip of the projectile for a Reynolds number ranging from $1 \times 10^5 \leq Re \leq 3.5 \times 10^6$ for $1 \leq r \leq 30$ mm. The coordinate r is directed along the cone surface and originates at the projectile's tip. Only the turbulent part of the boundary layer was considered, and transition phenomena have not been taken into account. The use of a transformation technique enables scaling of high-pressure conditions in the ballistic range, the so-called aerothermoballistic high-pressure test range, to actual atmospheric flight conditions. This facility allows duplication of the heating scenario during some seconds of atmosphere flight, with a flight in compressed gas resulting in the same heat flux for a flight time of some milliseconds. The transformation was validated using data from the range, obtained from the infrared surface emission at two wavelengths. Herewith the cone surface temperature is measured by detecting the intensity of the infrared emission coming from the cone surface.

Nomenclature

a_f	=	transfer factor
B	=	function of n
C_d	=	drag of projectile
c	=	heat capacity of projectile material
c_p	=	heat capacity of gas flow
n	=	constant factor
Pr	=	Prandtl number
p	=	static gas pressure
$\dot{q}$	=	heat flux
r, ϑ, φ	=	spherical coordinates
T	=	gas temperature
T_r	=	recovery temperature
t	=	time
u, v	=	velocity components
x, y	=	Cartesian coordinates
δ	=	boundary-layer thickness
δ^{**}	=	momentum thickness
λ	=	projectile material thermal conductivity
μ	=	dynamic viscosity
ν	=	kinematic viscosity
ρ	=	gas density
τ	=	skin friction
φ	=	factor concerning gas compressibility

Subscripts

c	=	flow around cone
e	=	flow outside of boundary layer (outer edge)
g	=	gas flow
p	=	projectile
w	=	cone surface (boundary)
∞	=	flow upstream of bow shock

Presented as Paper 2000-2516 at the AIAA 21st Aerodynamic Measurement Technology and Ground Testing Conference, Denver, CO, 19–22 June 2000; received 26 February 2001; revision received 10 July 2001; accepted for publication 11 July 2001.

*Professor, Shock Tube Department, 5, Rue du Général Cassagnou.
†Research Scientist, Accelerator Department, 5, Rue du Général Cassagnou.
‡Senior Scientist, Shock Tube Department, 5, Rue du Général Cassagnou.

I. Introduction

A PROJECTILE with a conical nose flying at Mach number $M_\infty > 1$ in the atmosphere develops a bow wave around its nose by which the incoming airflow is turned parallel to the projectile surface, as depicted in Fig. 1, in the reference frame of the projectile. The air is compressed, heated, and accelerated by the bow wave from upstream air pressure p_∞, upstream air temperature T_∞, and u_∞, which is equal to the projectile flight velocity u_p to the downstream parameters p_e, T_e, and u_e. Consequently, a heat flux develops from the hot air flow along the projectile surface that is directed into the inner of the projectile material. This heat flux causes a temperature increase. In particular, the nose of such a projectile can be extremely heated depending on the projectile speed, the flight time, the structure of the surface material, and its geometry.

The aim of our work is to model theoretically and experimentally the heating of a projectile and how it develops during its flight in the Earth's atmosphere. Surface temperature measurements in flight are very difficult to carry out. For this purpose, a special ground test facility was built that consists of an accelerator and a test tube in which the projectile under investigation is injected. This test tube contains the test gas under compressed conditions and ambient temperature. With a similarity law, the heating for a flight in the atmosphere at condition 1 and the flight in the test tube at condition 2 can be related to each other by Eq. (22), given in Sec. II.D., given the same heat flux development for both, for some seconds of atmospheric flight and flight in the test tube for some milliseconds.

In this test facility, called the aerothermoballistic high-pressure facility, the sharp-nosed body is flying at supersonic velocity through the test tube initially filled with a compressed gas, for example, air or nitrogen at ambient temperature. The incoming flow is heated by bow shock compression and directed parallel to the nose cone surface of the projectile, as is the case in Earth-atmosphere flight (see Fig. 1). At the cone surface a turbulent boundary layer develops for the flow velocity and gas temperature according to the existent

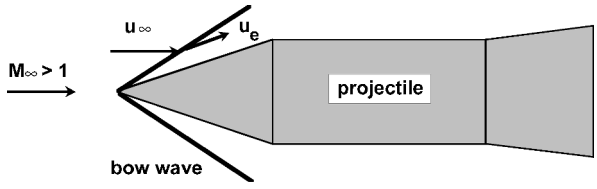

Fig. 1 Flow development in supersonic atmospheric flight.

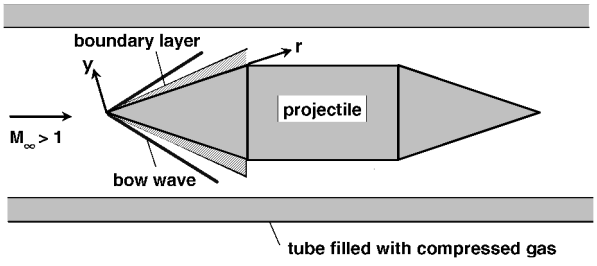

Fig. 2 Flow development in test tube flight.

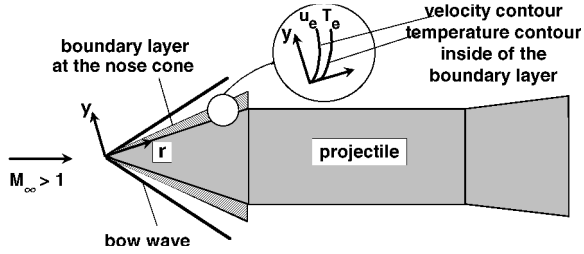

Fig. 3 Boundary layer at the nose cone.

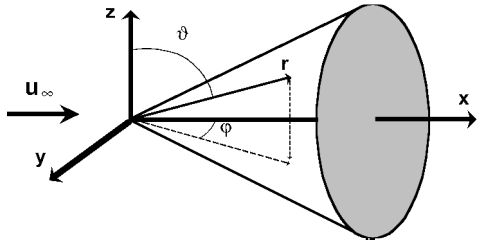

Fig. 4 Projectile's nose in spherical coordinates.

wall boundary conditions at the surface as well as at the outer edge of the boundary layer, as depicted in Fig. 2.

For calculation purposes, usually the whole conservation equations of mass, momentum, and energy have to be taken into account, including skin friction and heat conduction. Numerical methods have to be used to solve this complex system of differential equations. In this study, a fast running procedure was developed to find solutions from the conservation equations for the boundary-layer formation at the surface of a projectile in flight. We used the boundary-layer estimation of Prandtl (see Schlichting[1]) to get solutions in terms of analytical relations that are described in the next section.

II. Theory

A. Boundary-Layer Equations

Here we consider airflows at Reynolds numbers up to about 3.5×10^6. In that case, a thin boundary layer develops at the cone surface, where viscosity and heat conduction are important factors, and the boundary-layer theory can be applied for cone flow prediction. Across this layer the velocity increases from zero at the cone surface to the freestream velocity u_e. The gas temperature changes from the temperature T_w at the surface of the projectile nose to the gas temperature T_e inside the core flow as shown schematically in Fig. 3.

For a theoretical description of the formation of the boundary layer considered herein, the aforementioned system of conservation equations containing the mass, momentum, and energy equations have to be applied. The Reynolds number ranges from $1 \times 10^5 \leq Re \leq 3.5 \times 10^6$ for $1 \leq r \leq 30$ mm, and from there the transition from laminar to turbulent boundary-layer behavior occurs some millimeter downstream the tip of the projectile. The coordinate r is directed along the cone surface and originates at the projectile's tip (see Fig. 4). Transition phenomena have not been taken into account in this work, and only the turbulent part of the boundary layer was considered. Therefore, a turbulence model must be fitted into this set of conservation equations. It is difficult to find an analytical solution for this complex system of differential equations, and in most cases the solution must be found numerically. Compared with these efforts, an analytical solution is, due to some simplifications, less exact than the solution of the full set of conservation equations, but permits an understanding of the influence of important parameters. Therefore, a scheme for solving analytically Prandtl's boundary-layer equations has been developed for predicting the formation of the turbulent boundary layer at the surface of the projectile nose cone. The boundary-layer equations are considered in spherical coordinates, with the origin located at the tip of the projectile's nose (see Fig. 4). The instationary, time-dependent projectile flight was taken into account by a time-step procedure, as outlined by Seiler et al.[2] The real flight speed variation is approached at successive time intervals $\Delta t_0, \Delta t_1, \Delta t_2, \ldots, \Delta t_n = t_{n+1} - t_n$ with constant flow quantities during these steps, but that change with ongoing flight time. Therefore, the flow can be treated as stepwise time independent, and so the time dependence is withdrawn from Prandtl's boundary-layer equations.[1]

For finding a solution to Prandtl's boundary-layer equations,[1] these equations are transformed with the following relations:

$$\tilde{\chi} = \sqrt{3}\left[r(\vartheta - \vartheta_w)/\sqrt{r}\right] \tag{1a}$$

$$\bar{v} = \left(\sqrt{3}/\sqrt{r}\right)\left\{\bar{w}(\tilde{\chi}) - \tfrac{2}{3}\tilde{\chi}\bar{u}\right\} \tag{1b}$$

When Eqs. (1a) and (1b) are introduced in the boundary-layer equations, a new set of differential equations results. This procedure is explained in detail by Hantzsche and Wendt.[3] Because the boundary layer here becomes turbulent, the parameters considered in the conservation equations are written as time averaged mean values $\bar{\rho}$, $\bar{u}$, $\bar{v}$, and $\bar{T}$. For mass,

$$-\frac{\tilde{\chi}}{2}\frac{\mathrm{d}}{\mathrm{d}\tilde{\chi}}(\bar{\rho}\bar{u}) + \frac{\mathrm{d}}{\mathrm{d}\tilde{\chi}}(\bar{\rho}\bar{w}) = 0 \tag{2}$$

for momentum,

$$-\frac{\bar{\rho}\bar{u}\tilde{\chi}}{2}\frac{\partial\bar{u}}{\partial\tilde{\chi}} + \bar{\rho}\bar{w}\frac{\partial\bar{u}}{\partial\tilde{\chi}} = \frac{\partial}{\partial\tilde{\chi}}\left(\mu\frac{\partial\bar{u}}{\partial\tilde{\chi}}\right) \tag{3}$$

and for energy,

$$-\frac{\bar{\rho}\bar{u}\tilde{\chi}}{2}\frac{\partial}{\partial\tilde{\chi}}(c_p\bar{T}) + \bar{\rho}\bar{w}\frac{\partial}{\partial\tilde{\chi}}(c_p\bar{T}) = \frac{\partial}{\partial\tilde{\chi}}\left(\lambda\frac{\partial\bar{T}}{\partial\tilde{\chi}}\right) + \mu\left(\frac{\partial\bar{u}}{\partial\tilde{\chi}}\right)^2 \tag{4}$$

The differential Eqs. (2–4) have to be solved using the boundary conditions for temperature $\bar{T}$ and the velocity components $\bar{u}$ and $\bar{v}$, which are

$$\bar{T}(r, \vartheta_c) = T_c \tag{5a}$$

$$\bar{T}(r, \vartheta_w) = T_w \tag{5b}$$

$$\bar{u}(r, \vartheta_c) = u_c \tag{5c}$$

$$\bar{u}(r, \vartheta_w) = 0 \tag{5d}$$

$$\bar{v}(r, \vartheta_w) = 0 \tag{5e}$$

From a formal point of view, the Eqs. (2–4) are similar to the boundary-layer equations valid for the flat plate boundary layer. In

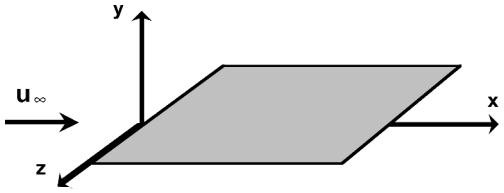

Fig. 5 Flat plate in Cartesian coordinates.

this case, the simplified conservation equations (see Schlichting[1]) are given in Cartesian coordinates (Fig. 5).

Transforming the plate boundary-layer equations with

$$\chi = y/\sqrt{x} \tag{6a}$$

$$\bar{v} = \tilde{\bar{v}}/\sqrt{x} \tag{6b}$$

gives the following new set of boundary-layer equations describing the boundary-layer formation on a flat plate. For mass,

$$-\frac{\chi}{2}\frac{\mathrm{d}}{\mathrm{d}\chi}(\bar{\rho}\bar{u}) + \frac{\mathrm{d}}{\mathrm{d}\chi}(\bar{\rho}\tilde{\bar{v}}) = 0 \tag{7}$$

for momentum,

$$-\frac{\bar{\rho}\bar{u}\chi}{2}\frac{\partial \bar{u}}{\partial \chi} + \bar{\rho}\tilde{\bar{v}}\frac{\partial \bar{u}}{\partial \chi} = \frac{\partial}{\partial \chi}\left(\mu\frac{\partial \bar{u}}{\partial \chi}\right) \tag{8}$$

and for energy,

$$-\frac{\bar{\rho}\bar{u}\chi}{2}\frac{\partial}{\partial \chi}(c_p\bar{T}) + \bar{\rho}\tilde{\bar{v}}\frac{\partial}{\partial \chi}(c_p\bar{T}) = \frac{\partial}{\partial \chi}\left(\lambda\frac{\partial \bar{T}}{\partial \chi}\right) + \mu\left(\frac{\partial \bar{u}}{\partial \chi}\right)^2 \tag{9}$$

Regarding the transformed Eqs. (2–4) for the cone boundary layer and Eqs. (7–9) for the plate boundary layer, we see that both systems appear to be equal. However, the difference between both can be found in the different meaning of coordinates χ for the plate and $\bar{\chi}$ for the cone. There are also differences in the velocity component definitions of $\tilde{\bar{v}}$ (plate) and $\bar{w}$ (cone).

The similarity between the transformed cone boundary-layer Eqs. (2–4) and those for the plate boundary layer, Eqs. (7–9), shows that with a solution for the plate boundary-layer formation and the coordinate transformations in Eqs. (1) and (6), the cone boundary layer and the plate boundary layer can be related to each other. Hantzsche and Wendt[2] gave some data on these relations concerning laminar boundary-layer development. In our case the flow is turbulent, and the transfer factor was determined with data given by Chien.[4] From the considerations discussed on the similarity between the cone and plate boundary-layer equations, there is justification for solving the plate boundary-layer Eqs. (2–4) instead of the more complex cone boundary-layer Eqs. (7–9). However, the results must be transformed to the given cone geometry by using appropriate transfer data (see Chien[4]).

A solution for the plate boundary-layer equations using an integral approach can be found in Ref. 1 by determining some integral data which are obtained by integration of the boundary-layer equations along the coordinate y inside of the boundary-layer thickness. Integration of the momentum equation for the flat plate boundary layer from $y = 0$ (wall) up to $y = \delta$ (outer edge of the boundary layer) gives

$$\int_{y=0}^{\delta}\left(\bar{\rho}\bar{u}\frac{\partial \bar{u}}{\partial x} + \bar{\rho}\bar{v}\frac{\partial \bar{u}}{\partial y}\right)\mathrm{d}y = -\tau_w \tag{10}$$

with

$$\tau_w = \mu\left(\frac{\partial \bar{u}}{\partial y}\right)_w \tag{11}$$

When the velocity component $\bar{v}$ in Eq. (10) is replaced using the conservation of mass equation, then for the wall shear stress τ_w equation along the plate's coordinate x the following integral relation is obtained (see Oertel[5]):

$$\tau_w = \frac{\mathrm{d}}{\mathrm{d}x}\int_0^{\delta}\bar{\rho}\bar{u}(\bar{u}_e - \bar{u})\,\mathrm{d}y + \frac{\mathrm{d}\bar{u}_e}{\mathrm{d}x}\int_0^{\delta}(\rho_e\bar{u}_e - \bar{\rho}\bar{u})\,\mathrm{d}y \tag{12}$$

In turbulent boundary layers, velocity profiles are described approximately by the power-law equation as discussed by Schlichting[1]:

$$\bar{u}/\bar{u}_e = (y/\delta)^{1/n}, \qquad 5 \le n \le 10 \tag{13}$$

When Eq. (13) is introduced into Eq. (12), a relation for the boundary-layer thickness δ as a function of x along the plate is obtained:

$$\frac{\tau_w}{\rho_e\bar{u}_e^2} = \frac{\delta^{**}}{\delta}\frac{\mathrm{d}\delta}{\mathrm{d}x} \tag{14a}$$

With a relation given by Schlichting[1] for turbulent flows, as

$$\tau_w \big/ \rho_e\bar{u}_e^2 = B(n)\varphi(\nu_e/\bar{u}_e\delta)^{2/(n+1)} \tag{14b}$$

the following differential equation can be found:

$$B(n)\varphi\left(\frac{\nu_e}{\bar{u}_e\delta}\right)^{2/(n+1)} - \frac{\delta^{**}}{\delta}\frac{\mathrm{d}\delta}{\mathrm{d}x} = 0 \tag{14c}$$

The factor B is given by Schlichting[1] for $n = 5$, as $B(n) = 0.0488$; $n = 6$, $B(n) = 0.0313$; $n = 7$, $B(n) = 0.0225$; $n = 8$, $B(n) = 0.0176$; $n = 9$, $B(n) = 0.0143$; and $n = 10$, $B(n) = 0.0118$.

Equation (14c) is solved with the outer core flow conditions, that is, flow speed u_e, pressure p_e, and temperature T_e. With the Reynolds analogy,

$$\dot{q}_g = c_p(T_r - T_w)Pr^{-\frac{2}{3}}\tau_w \big/ \bar{u}_e \tag{15}$$

the analytical solution for predicting the heat flux $\dot{q}_g$ at the surface as a function of the coordinate x along the surface of the flat plate is given as

$$\dot{q}_g(x) = a_f[(n+1)/(n+3)]^{2/(n+3)}[B(n)\varphi]^{(n+1)/(n+3)}c_p(T_r - T_w)$$

$$Pr^{-\frac{2}{3}}\bar{\rho}_e(\delta^{**}/\delta)^{2/(n+3)}\bar{u}_e^{(n+1)/(n+3)}(\nu_e/x)^{2/(n+3)} \tag{16}$$

All of the parameters used in Eq. (16), such as n, $B(n)$, φ, δ, δ^{**}, T_r, T_w, c_p, $\bar{\rho}_e$, and ν_e are defined in the Nomenclature and more in detail by Seiler.[6] Equation (16) works for a perfect gas, not including real gas effects such as vibration, dissociation, and so on, that are not present in the study considered herein. When taking into account the heat flux $\dot{q}_g$ to the sharp-cone geometry of the projectile nose, the calculated flat plate heat flux of Eq. (16) is changed to cone geometry using the transfer factor a_f with $a_f > 1$ and the plate coordinate x is transformed into the cone coordinate r. A theoretical estimation of this factor is not available for turbulent flows. For determining a_f and the heat flux $\dot{q}_g$, Eq. (16) is fitted to the experimental heat transfer results of Chien,[4] which were obtained at hypersonic flow conditions, as in the present study. The experiments of Chien[4] have been performed in a wind tunnel using a sharp cone with a 5-deg cone half-angle at a freestream Mach number $M_\infty = 7.9$. The best agreement with Eq. (16) is found with $a_f = 1.07$ using $n = 9$. It may be that the factor a_f is additionally a function of the cone half-angle, and this dependence should be taken into account in future work to obtain a more exact prediction of the factor a_f.

B. Heat Conduction Equation

The heat flux $\dot{q}_g(x)$ calculated from Eq. (16) is found to be, practically speaking, little dependant on the plate's coordinate x, that is, the cone's surface coordinate r. Therefore, the one-dimensional heat conduction equation was applied in depth y inside the wall region at each location r along the cone surface:

$$\frac{\partial T}{\partial t} = k\frac{\partial^2 T}{\partial y^2}, \qquad \text{with} \qquad k = \frac{\lambda}{\rho c} \tag{17}$$

By integration of Eq. (17) with the given boundary conditions,

$$\Delta T(y, t < 0) = \Delta T(\infty, t) = 0, \qquad \frac{\partial T}{\partial y}(0, t > 0) = \frac{-\dot{q}(0, t)}{\lambda} \tag{18a}$$

an analytical solution for the temperature change ΔT_w at the cone as a function of the heat flux $\dot{q}_w(x)$ can be obtained from a 1997 private communication with F. Gatau at the French–German Research Institute of Saint-Louis (ISL) as

$$\Delta T_w(x, y, t) = \frac{\dot{q}_w(x)}{\sqrt{\rho c \lambda}} \times \left[2\frac{\sqrt{t}}{\sqrt{\pi}} \exp\left(-\frac{y^2}{4kt} \right) - \frac{y}{\sqrt{k}} \operatorname{erfc}\left(\frac{y}{2\sqrt{kt}} \right) \right] \tag{18b}$$

The analytical solution in Eq. (18b) is applied for calculating the temperature distribution $T_w(x, y, t)$ inside of the projectile nose as a function of the heat flux $\dot{q}_g(x)$. When $\dot{q}_g(x)$ of Eq. (16) is introduced in Eq. (18) by assuming that the heat flux at the surface at $y = 0$ is equal for both the gas and the wall side, with

$$\dot{q}_g(x) = \dot{q}_w(x, y = 0) \tag{19}$$

the temperature distribution

$$T_w(x, y, t) = T_0 + \Delta T_w(x, y, t) \tag{20}$$

inside the nose cone material can be calculated, where λ is the material heat conductivity, ρ its density, and c its specific heat. The parameter t denotes the flight time, which was subdivided into n time steps. For each of the steps, the flow is considered to be a stationary one.

C. Presentation of Different Flight Scenarios

In case of projectile speed diminution by drag C_d, the time dependence was modeled by stepwise application of the procedure described in Sec. II.B along the flight cycle in the atmosphere as well as in the ballistic range facility.[7] Four different flight scenarios have been calculated to demonstrate the range of temperature increase at the nose of a projectile in flight. The projectile types considered are: 1) a German high-speed (HFK) projectile with mass = 120 kg and $C_d = 0.35$; 2) a 120-mm kinetic energy (KE) projectile with mass = 4 kg and $C_d = 0.35$; 3) a 30-mm full projectile with mass = 360 g and $C_d = 0.20$; and 4) a 155-mm full projectile with mass = 45 kg and $C_d = 0.20$.

The flight trajectory was calculated for each of the four projectile types with the assumption of constant projectile drag C_d and sea-level conditions. The result for the projectile speed u_p vs flight time is given in Fig. 6 with two time coordinates. The upper one is valid for the HFK projectile, the KE projectile, and the 30-mm caliber full projectile. The lower one is only valid for the 155-mm full caliber projectile.

In Fig. 7, the cone surface temperature variation at location $r = 10$ mm from the cone tip is drawn as a function of the flight

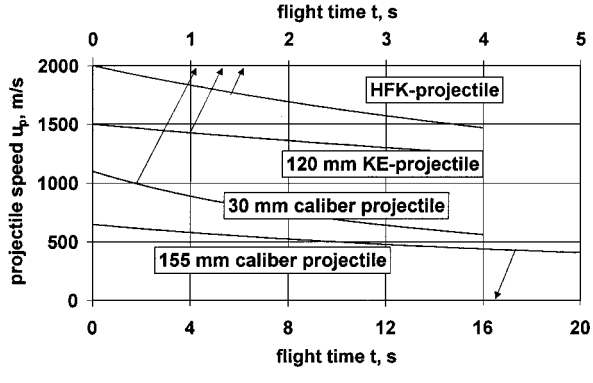

Fig. 6 Projectile speed scenario vs flight time.

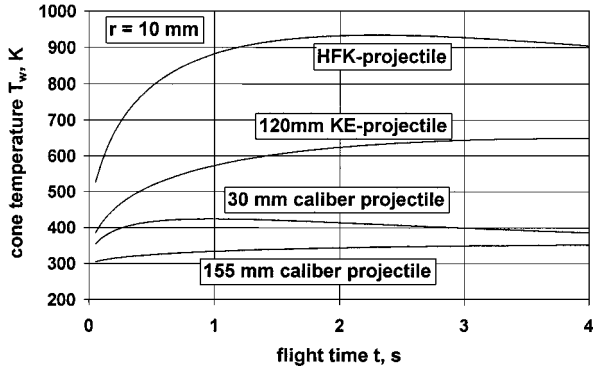

Fig. 7 Nose cone heating at $r = 10$ mm from nose tip.

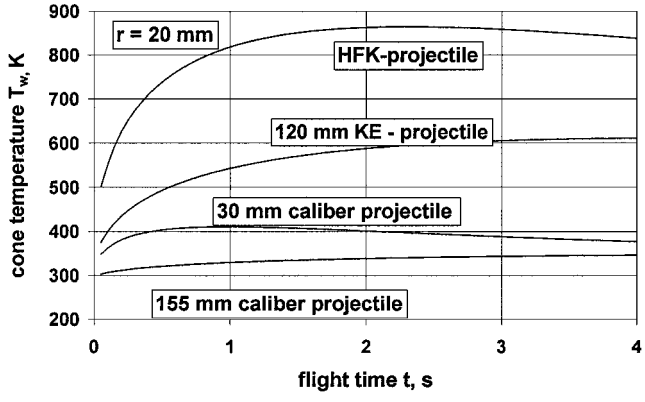

Fig. 8 Nose cone heating at $r = 20$ mm from nose tip.

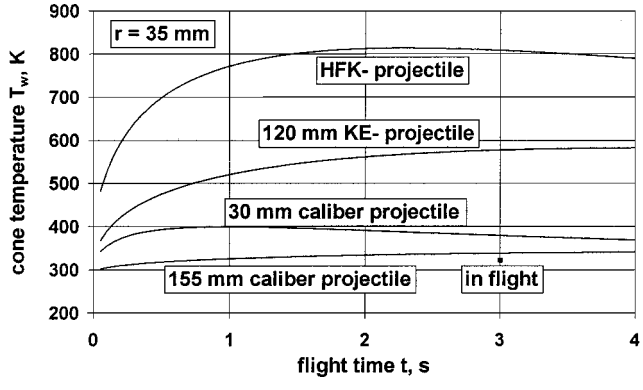

Fig. 9 Nose cone heating at $r = 35$ mm from nose tip.

time for the four projectile types considered. For all cases it is assumed that the nose is made of steel with density $\rho = 7840$ kg/m^3, specific heat $c = 458$ J/kg K, and heat conductivity $\lambda = 50$ W/m K. For the HFK projectile, a maximum temperature of about 940 K is reached after a flight time of 2 s. The 120-mm subcaliber KE projectile is heated to about 650 K during 4-s flight time. A lower surface temperature is calculated for the 30-mm full caliber projectile. Here we obtain from Fig. 7 a maximum temperature of 420 K after a 1-s flight. The 155-mm caliber projectile maximum cone surface temperature is in the range of 350 K after a flight of 3 s. The 120- and 155-mm profiles show a monotonous increase with no maximum, as have the HFK and 30-mm distributions. The reason for this development is that the timescale in Fig. 7 of a maximum of 4 s is too short to show the maximum for both the 120- and 155-mm caliber temperature distributions that occur at longer flight times, not discussed herein.

Similar temperature histories develop for the position $r = 20$ mm from the nose tip (Fig. 8), as well as for $r = 35$ mm (see Fig. 9). Additionally, in Fig. 9 the result of a thermocouple measurement in flight is introduced for the 155-mm full caliber projectile.[8] The

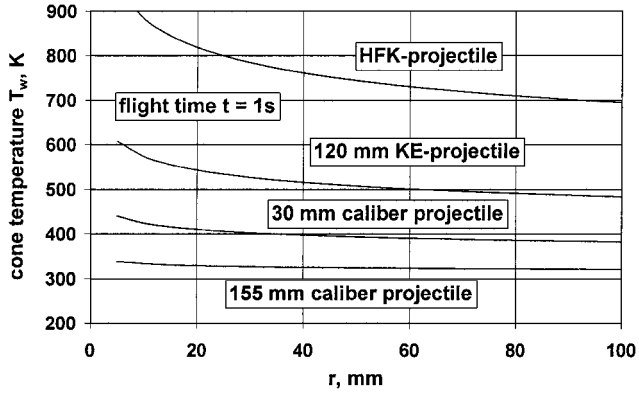

Fig. 10 Nose cone heating at flight time $t = 1$ s.

temperature measured is in very good agreement with the theoretical prediction. It must be taken into account that the thermocouple was not made of steel used for the calculation of the cone heating. Therefore, some differences between measurement and theory must appear.

The temperature distribution along the cone surface is given in Fig. 10 for a flight time of 1 s. We see the same temperature development as discussed earlier, with the HFK projectile nose strongly heated, a much lower heating for the KE projectile, then the 30-mm caliber projectile, and the lowest heating for the 155-mm full caliber projectile. The outcome of this diagram shows a temperature increase toward the nose tip, which theoretically goes to infinity for $r = 0$.

D. Transformation Equation

The goal of our investigations is to model in the aerothermoballistic high-pressure range facility the heat flux present in flight at the nose of a projectile. Relating the real flight condition 1 and the modeling conditions in our test facility (condition 2) with Eq. (16) requires the condition of equal integral heat flux during the flight time t:

$$\int_{t=0}^{t} \dot{q}_{g,1}(x)\,\mathrm{d}t = \int_{t=0}^{t} \dot{q}_{g,2}(x)\,\mathrm{d}t \tag{21}$$

Then, for different flight cycles in the atmosphere for condition 1 and in our ground testing facility for condition 2, Eq. (21) can be fulfilled if the condition in Eq. (22),

$$p_1 f_1(u_1, t_1) = p_2 f_2(u_2, t_2) \tag{22}$$

for pressure p_1 and p_2, as well as for the functions f_1 and f_2, is balanced. The functions f_1 and f_2, must be calculated stepwise in time from Eq. (22). In the case of constant projectile speeds u_1 and u_2, Eq. (22) evaluates as

$$p_1\sqrt{t_1} = p_2\sqrt{t_2} \tag{23}$$

This result means that the conditions in the ballistic range facility (i.e., gas pressure p_2 and test flight time t_2) must be calculated according to Eq. (22) using the given atmospheric pressure p_1 and the real flight time t_1.

III. Experiments

A. Aeroballistic Range Facility

In the aerothermoballistic range facility the bow wave heating at the nose of a projectile, flying during several seconds t_1 some kilometers in the lower atmosphere at $p_1 \approx 0.1$ MPa (normal pressure) can be modeled in compressed gas p_2 with a flight time t_2 of some milliseconds. This facility consists of a powder gun for accelerating the projectiles to a muzzle velocity up to 2000 m/s, followed by a test tube in which the projectile models are injected (see Fig. 11). The acceleration tube is seen on the right-hand side of Fig. 11.

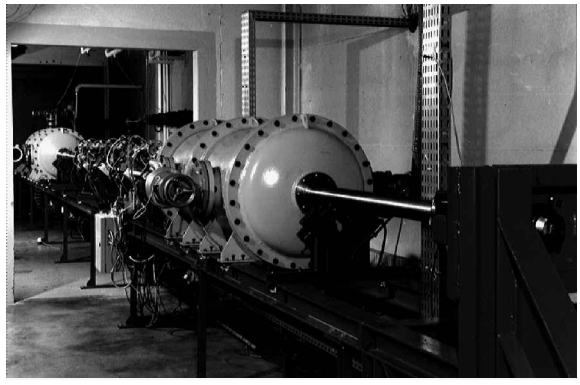

Fig. 11 Powder gun, two tanks, and rail tube in between.

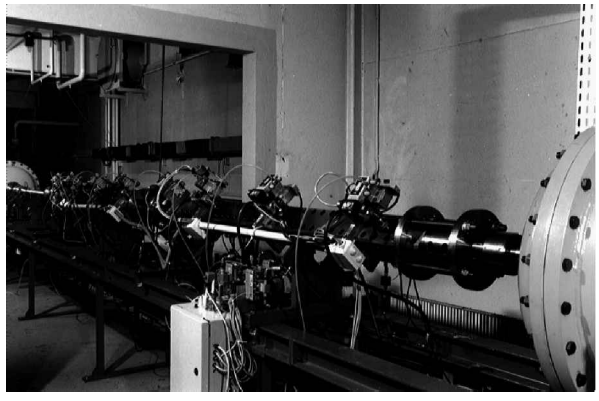

Fig. 12 View on rail test tube with equipment.

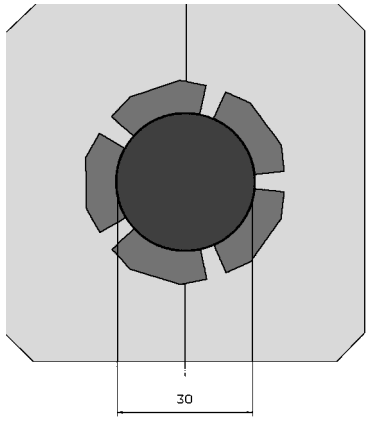

Fig. 13 Cross section of rail test tube with five rails.

The test tube placed between the two dump tanks is seen in Fig. 12 with all of the equipment necessary for operation: 1) valves for gas filling, 2) pressure gauges for wall pressure measurement, and 3) electromagnetic sensors for determination of projectile position. This compression tube has a length of about 5 m and is closed by diaphragms at both ends. A detailed description of the facility is given by Seiler et al.[2] The test tube is designed as a two-caliber tube having five inner rails for projectile guiding (see Fig. 13) and is filled with compressed gas in the range of up to 8 MPa. The outer caliber is 44 mm and the inner rail caliber is 30 mm. A cross section of this high-pressure rail tube is given in Fig. 13. In the decelerator tube at the end of the facility, a piston is located, equipped with inner replaceable steel plates for projectile catching (Fig. 14). An impact on these steel plates can be seen in the photograph in of Fig. 15.

As an example of the conditions in our high-pressure ground testing facility, with a flight time of about 3 ms, the fill pressure must be higher than atmospheric pressure to model the same heat flux at the projectile cone surface as is present for atmospheric air

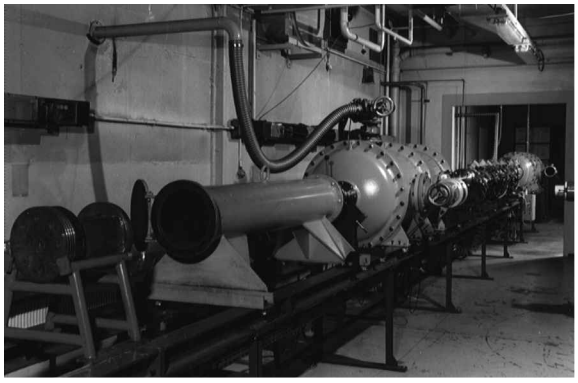

Fig. 14 Decelerator tube with catching piston.

Fig. 15 Catching piston with projectile impact.

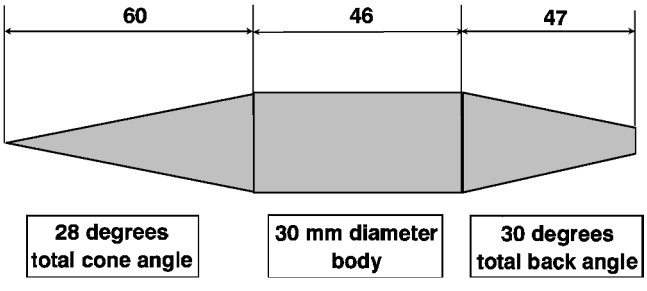

Fig. 16 Geometry of projectile used.

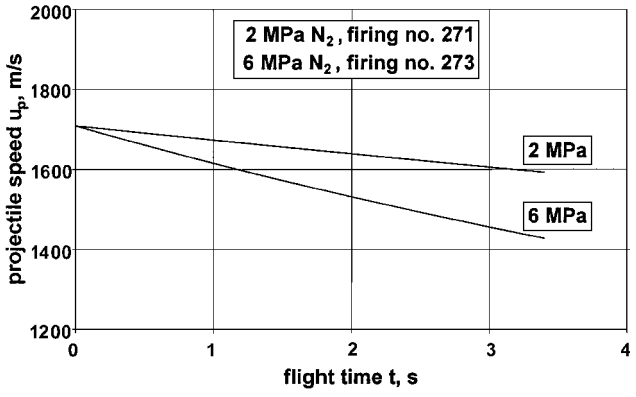

Fig. 17 Speed distribution in high-pressure test tube.

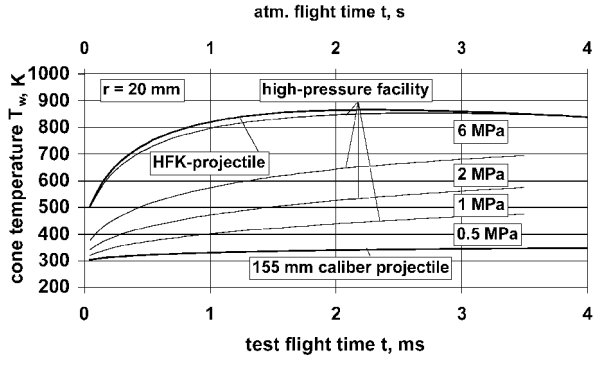

Fig. 18 Projectile nose heating in the test facility: upper scale, HFK and 155-mm projectiles and lower scale, others.

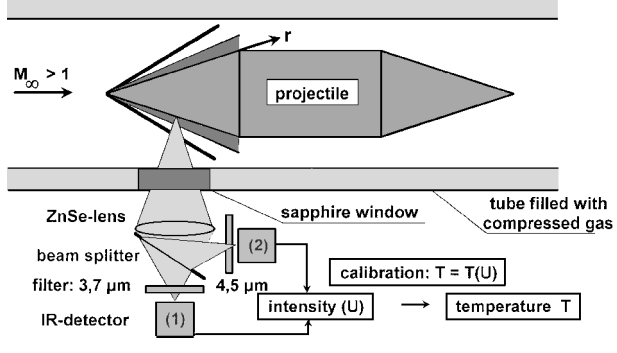

Fig. 19 Pyrometric measurement.

flight. With Eq. (23) we calculate a test gas pressure of about 2 MPa for a 1-s atmospheric flight at sea-level conditions.

B. Firings Performed

In our high-pressure ground testing facility, we fired projectiles with a mass of about 150 g, with a projectile speed of about 1730 m/s, into the high-pressure test tube. The projectile is designed with a solid magnesium body that is equipped with a full 28-deg steel nose cone. The projectile dimension in millimeters is presented in Fig. 16 showing the fore-, the mid-, and the afterbody.

Test firings have been performed in 2-, 4-, 6-, and 8-MPa N_2 atmospheres. Because of projectile drag, the projectile speed u_2 decreases during the flight time t_2, that is, $u_2 = u_2(t_2)$. As an example, in Fig. 17 the projectile speed diminution is shown for firing number 271 in a 2-MPa compressed N_2 atmosphere, and for number 273 in 6-MPa N_2. A velocity decrease of several hundred meters per second develops, and, therefore, the square root time dependence in Eq. (23) can only be applied approximately. Of course, the flow around the projectile becomes unsteady, and some deviations to Eq. (23) appear. In this case more exact calculations have been performed using the stepwise procedure, mentioned in Sec. II.C, to predict the function $f_2 = f_2(u_2, t_2)$ in Eq. (22).

The nose cone temperature histories calculated for the heating during projectile flight inside of our ground testing facility are depicted in Fig. 18 for filling pressures of 0.5-, 1-, 2-, and 6-MPa N_2. The timescale is in milliseconds (lower scale) for the test flight time and in seconds (upper scale) for the HFK and the 155-mm projectile atmospheric flight. The outcome shows that in case of 6-MPa N_2 in the ground testing facility the nose temperature increase is comparable with that given for an HFK projectile. For lower cone surface temperatures, as are present in flight of a 155-mm full caliber projectile, the fill pressure in our high-pressure test tube has to be adapted to less than 0.5 MPa. In varying the fill pressure p_2, a wide range of heating scenarios can be modeled, beginning at low surface temperatures for, for example, a 155-mm full caliber projectile up to temperatures present on the surface of high-speed projectiles (Fig. 18).

C. Surface Temperature Measurement

For surface temperature measurement we detected the intensity of the steel surface emission at wavelengths of 3.7 and 4.5 μm. Two wavelength measurements are chosen for comparing and controlling both measurements with each other. This surface emission is registered, as outlined in Fig. 19, through a sapphire window placed near

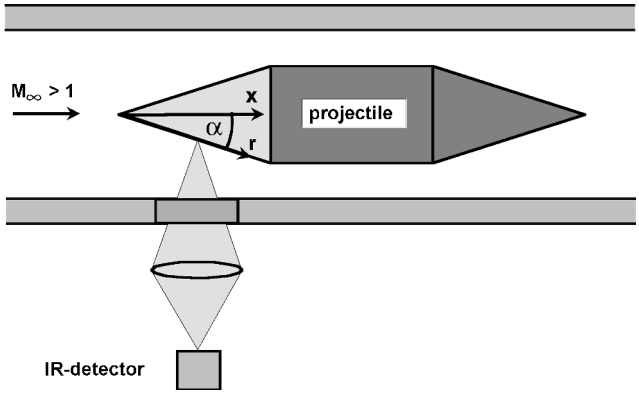

Fig. 20 Geometry for cone, $\cos\alpha = x/r$.

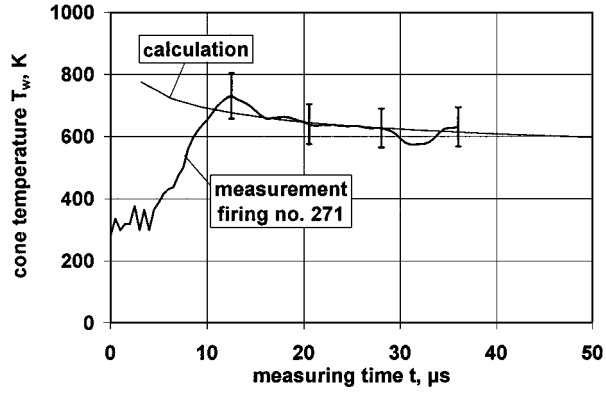

Fig. 21 Comparison of experiment and theory for 2-MPa fill pressure.

the tube end using fast infrared detectors at the time of projectile passing.

The recorded detector output signal is given as voltage U vs measuring time t: $U = U(t)$. With a calibration curve $T = T(U)$ (see Seiler et al.[7]) the surface temperature T can be evaluated vs the measuring time t of projectile passage at the measuring port, that is, the sapphire window, resulting in $T = T(t)$. Given practically constant speed for the projectile passage at the measuring station (sapphire window), the timescale t can be transformed in length scale x as $x = u_p t$ and with Eq. (24) in the coordinate r along the cone surface:

$$r = u_p t/\cos\alpha \tag{24}$$

Figure 20 shows the projectile nose geometry with the coordinates x along the projectile axis and r along the cone surface.

IV. Comparison of Theory and Experiment

The measured surface temperatures are compared with corresponding theoretical predictions for the four firings: firing number 271 with 2-MPa N_2 in Fig. 21, firing number 272 with 4-MPa N_2 in Fig. 22, firing number 273 with 6-MPa N_2 in Fig. 23, and firing number 274 with 8-MPa N_2 in Fig. 24. We used N_2 as test gas instead of air (21% O_2 + 79% N_2) because the radiation of excited O_2 molecules may disturb the infrared (IR) emission coming from the cone surface, giving a nonnegligible measuring error. N_2 molecules behave inertly, having practically the same physical gas nature as air only. The experimental results included in Figs. 21–24 are given for the 3.7-μm wavelengths emission.

The field signals in Figs. 21–24 increase in the first 10–20 μs, and so they do not follow anywhere close to the theoretical line. The reason for that signal behavior is that the temperature measurement starts at the tip of the projectile with zero surface emission just at the tip of the projectile nose. Emission and measuring signal are fully established in case the measuring volume is fully located at the cone surface. Another outcome is that the temperature at the cone surface increases with increasing fill pressure p_2. The theoretical predictions show similar behavior. For firing number 271 in 2-MPa

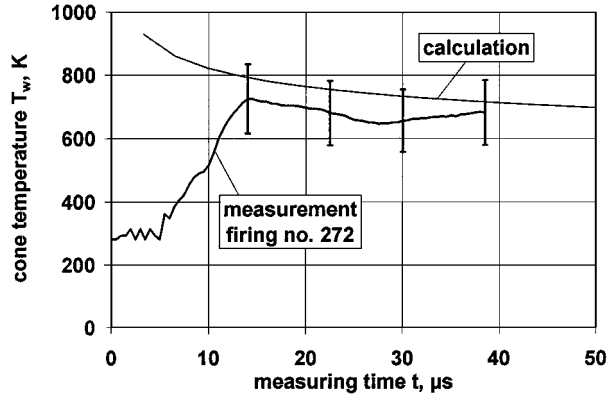

Fig. 22 Comparison of experiment and theory for 4-MPa fill pressure.

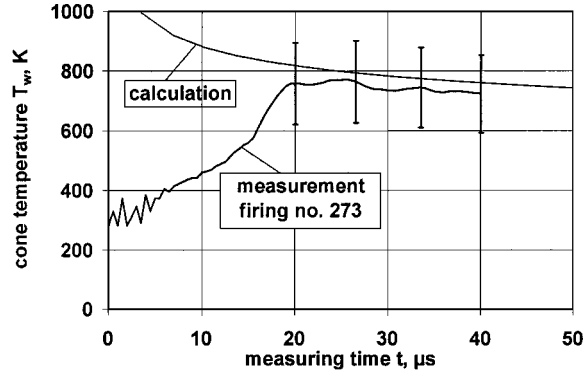

Fig. 23 Comparison of experiment and theory for 6-MPa fill pressure.

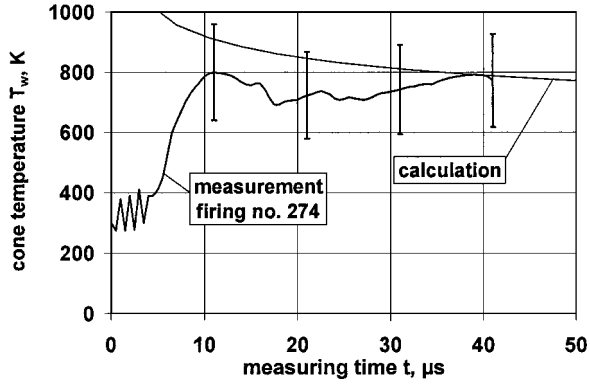

Fig. 24 Comparison of experiment and theory for 8-MPa fill pressure.

N_2, the comparison between experiment and theoretical prediction is well established (see Fig. 21). With increasing fill pressure, the temperature difference between calculated temperature distributions and measured ones increases. The reason for this deviation is not quite clear up to now. It may be found in the effect of light refraction occurring at the bow wave formed around the nose cone of the projectile. From Fig. 19, it can be seen that the light emitted from the cone surface passes the bow wave, passing, therefore, a density jump given by the bow shock wave. With increasing fill pressure, this density jump across the bow wave increases and along with it the refractive index jump. An increasing refractive index difference causes an increasing distortion of the path of the light bundle from surface to detector. This light distortion should be more or less compensated, because the light is focused by a lens on the IR detector. This optical problem is not solved yet and must be taken into consideration for future investigations to decrease the measuring error with increasing fill pressure.

The relative measuring error occurring for the temperature distributions in Figs. 21–24 is assumed to be as follows: Fig. 21, 10%; Fig. 22, 15%; Fig. 23, 18%; and Fig. 24, 20%.

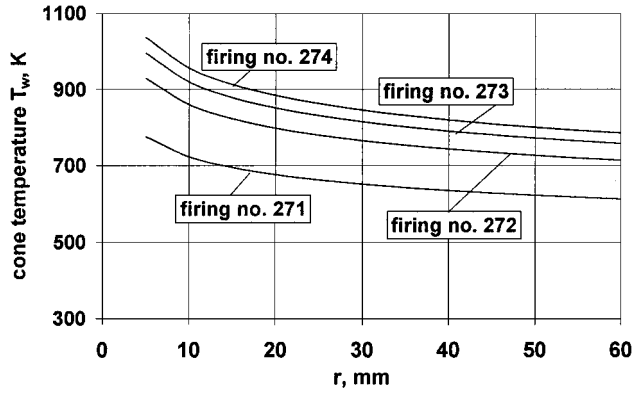

Fig. 25 Comparison of predicted surface temperatures.

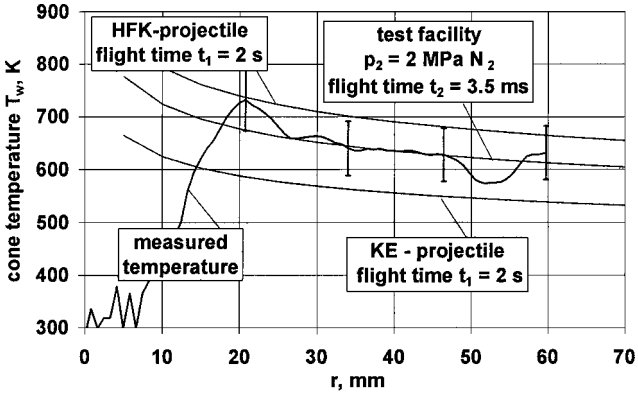

Fig. 26 Comparison of experiment and theory.

As discussed for Fig. 21, light refraction problems are negligible for the pressure condition of $p_2 = 2$ MPa fill pressure. Here, the measured and calculated surface temperatures are in good agreement, and so it can be assumed that the theory for predicting the temperature development at the nose of a projectile flying in our test facility can be used successfully and can also be applied for predicting the projectile heating during atmospheric flight.

Figure 25 gives a direct comparison of the predicted temperature distributions along the cone surface for the four fill pressure cases: 2, 4, 6, and 8 MPa. Increasing the fill pressure causes higher heat fluxes as outlined before, thereby giving higher surface temperatures. Adapting the fill pressure p_2 according to Eq. (22) to the flight scenario of interest, this scenario can experimentally be reproduced in our test facility, as outlined in Fig. 18. The application of the transformation law in Eq. (22) established for the operation of our high-pressure testing facility can be confirmed considering the following explanations for Fig. 26, which compares a measured temperature distribution with calculated ones for real flight scenarios.

For this purpose, a comparison of the experimental results of firing number 271 using a steel projectile nose with three calculated temperature distributions is given in Fig. 26. A direct comparison of experiment and theory as outlined for Fig. 21 is given by means of the calculated temperature distribution for $p_2 = 2$ MPa and $t_2 = 3.5$ ms. Additionally, two temperature distributions coming from Fig. 10 are included, that is, for an HFK projectile and for a KE projectile. This outcome confirms that our high-pressure ground testing facility has the capability to model the heating of a projectile during its atmospheric flight of some seconds with a flight in compressed gas of some milliseconds.

V. Summary

A ground testing facility was designed and built for modeling the real heat transfer at the conical nose of a projectile flying in the atmosphere. In this ballistic range the projectile is traveling through a compressed gas to obtain within some milliseconds the same surface heating as is present during an atmospheric flight of some seconds. To date, this high-pressure test range facility is unique worldwide for modeling this phenomena. With the similarity law of Eq. (22), the heating for the flight of some seconds t_1 in the atmosphere at pressure p_1 and that for the model flight time of some milliseconds t_2 in the test tube at a higher pressure p_2 are equal if Eq. (22) is applied for determination of pressure p_2 for modeling a desired flight scenario. Up-to-date hypersonic reentry or hypersonic flights in Earth's atmosphere is usually tested in nozzle flows. However, their frozen flow conditions lead to significant mismatching between ground test results and real flights. With this so-called aerothermoballistic high-pressure test facility a ballistic range technique was developed to have a ground testing facility in which the nose heating scenario during Earth-atmosphere flight can be measured.

For calculating the temperature distribution at the surface, it is assumed that a compressible and turbulent boundary layer develops at the conical projectile nose surface behind the bow wave. With Prandtl's boundary-layer equations, a theoretical model has been developed to calculate the boundary-layer development as well as the heat flux from gas to surface. With an analytical solution resulting from the heat conduction equation, the temperature distribution at the cone surface and in depth is calculated.

We investigated the projectile nose heating using steel as nose material at flight velocities up to about 1700 m/s in compressed nitrogen flows at gas pressures up to 8 MPa. The tube used has a length of about 5 m with an inner two-caliber bore: The outer caliber is 44 mm and the inner rail caliber is 30 mm for projectile guiding. To measure the surface temperature, we look for the cone surface emission at wavelengths of about 3.7 and 4.5 μm, respectively. This surface emission is registered through a sapphire window placed near the tube muzzle using fast IR detectors at the time of projectile passing: $U = U(t)$. The surface temperature T is given by a calibration function $T = T(U)$ as a function of the surface emission.

An example of the capability of our aerothermoballistic test facility is given in Fig. 26, with a comparison of the temperature distribution along the projectile's nose cone fired in this facility with two atmospheric flight cycles: 1) an HFK projectile flight and 2) the flight of a KE projectile. The real surface temperature range is reached for the HFK projectile as well as for the KE projectile.

Acknowledgments

The authors would like to express their gratitude to Günter Smeets and Hans Mach, both retired from the French–German Research Institute of Saint-Louis (ISL) since 1999, for the suggestion and the development of the pyrometric measuring technique used herein and for many fruitful discussions on this topic during their scientific work at ISL.

References

[1] Schlichting, H., *Boundary-Layer Theory*, McGraw–Hill, New York, 1960.

[2] Seiler, F., Gatau, F., and Mathieu, G., "Prediction of Surface Heating of a Projectile Flying in RAMAC 30 of ISL," *Third International Workshop on Ram Accelerator*, Tohoku University, Sendai, Japan, 1997.

[3] Hantzsche, W., and Wendt, H., "Die laminare Grenzschicht bei einem mit Überschallgeschwindigkeit angeströmten nichtangestellten Kreiskegel," *Jahrbuch der Deutschen Luftfahrtforschung I*, Zentrale für Wissenschaftliches Berichtswesen de Luftfahrtforschung, Berlin, 1941, pp. 76, 77.

[4] Chien, K.-Y., "Hypersonic, Turbulent Skin-Friction and Heat-Transfer Measurements on a Sharp Cone," *AIAA Journal*, Vol. 12, No. 11, 1974, pp. 1522–1526.

[5] Oertel, H., *Stoßrohre*, Springer-Verlag, Vienna, 1966.

[6] Seiler, F., "Theoretische und Experimentelle Untersuchung der Turbulenten Grenzschicht hinter einem Kolben im Stoßrohr," Habilitationsschrift and French–German Research Inst. of Saint-Louis Rept. 115/93, Saint-Louis, France, 1993.

[7] Seiler, F., Mach, H., Werner, U., Patz, G., and Smeets, G., "Theoretical and Experimental Investigation of Bow Wave Heating at the Conical Nose of Projectiles," *Proceedings of the 22nd International Symposium on Shock Waves*, Vol. 2, edited by G. J. Ball, R. Hillier, and G. T. Roberts, University of Southampton, Southampton, England, U.K., 1999, pp. 1567–1570.

[8] Gnemmi, P., Sommer, E., Naumann, K. W., and Fleck, V., "Aerothermal Study of a Projectile in Flight: Experiment-Computation Comparison," *Proceedings of the 18th International Symposium and Exhibition on Ballistics*, Vol. 1, edited by W. G. Reinecke, Technomic, Lancaster, PA, 1999, pp. 94–101.